Image Guidance and Safe Insertion Region Localization for Lumbar Puncture using Ultrasound

by

Aabha Tamhankar

A Thesis

Submitted to the Faculty

of the

WORCESTER POLYTECHNIC INSTITUTE

In partial fulfillment of the requirements for the

Degree of Master of Science

in

Robotics Engineering Department

_____

April 2024

APPROVED BY:

_____

Dr. Christopher Nycz, Advisor

_____

Dr. Haichong Zhang, Robotics Engineering Department, WPI

_____

Dr. Yihao Zheng, Mechanical Materials Engineering Department, WPI

Acknowledgements

I am thankful to my research advisor, Professor Christopher Nycz, for introducing me to the topic of this thesis, his unwavering support, guidance, and constructive feedback throughout my thesis journey. I also wish to thank Girivaasan Chandrashekharan for sharing insights on the project and being a part of it. Thank you to the everyone at PracticePoint, WPI, especially Xihan Ma, Kehan Yang and Andrew Daudelin, who provided guidance on the handling of devices and software necessary for my work. A heartfelt thank you goes to the faculty members and advisors, including special thanks to Professor Haichong Zhang and Professor Yihao Zheng for their mentorship and support as committee members during my thesis defense. Their expertise and constructive feedback have greatly enriched my research journey, and I am truly grateful for the privilege of learning from them.

To my family and friends, your constant encouragement and understanding have been my pillars of strength. I extend my appreciation to my peers and colleagues for all the stimulating discussions and collaborative efforts, that made this academic environment enriching and enjoyable. Special thanks to Worcester Polytechnic Institute for providing the necessary resources, facilities, and opportunities that have facilitated my research process and contributed to the overall success of this thesis. I extend my heartfelt thanks to all those who have been a part of my academic journey. Your collective support has shaped the outcome of this thesis, and I am truly grateful for the privilege of learning and growing in this academic community.

Abstract

Lumbar Puncture is a process in which a needle is inserted between two lumbar vertebrae, to access cerbrospinal fluid. While the use of ultrasound for vizualization is common, it is often noisy and fails to provide a complete view of the region. This thesis advances lumbar puncture techniques by integrating motion tracked 2D ultrasound and 3D MRI imaging, for providing visualization of the interspinal spaces of the lumbar vertebrae. We create a method where point clouds derived from ultrasound scans of the lumbar spine are registered with a volumetric MRI ground truth model. This facilitates the determination of safe needle insertion zones, which are then dynamically displayed on the ultrasound screen. This approach has the potential to aid clinicians real-time during LP procedures, which may result in reduced risk of procedural complications. Our work represents starting point towards enhanced image guided lumbar puncture. In this thesis, we present a framework for localizing valid trajectories based on acquired ultrasound images by using an MRI ground truth as guidance. The proposed pipeline, upon capturing an ultrasound image, is designed to determine the closest needle puncture location specified within the MRI ground truth point cloud.

Table of contents

List of figures

Chapter 1

Introduction

Lumbar Puncture (LP), also known as Spinal Tap, is a medical procedure performed to access the cerebrospinal fluid (CSF) for diagnostic or therapeutic purposes. This procedure involves inserting a needle between the lumbar vertebrae into the spinal canal. While primarily used to diagnose conditions like meningitis and multiple sclerosis, LP is also used in administering medications directly into the CSF. In contrast, an epidural injection targets the epidural space around the spinal cord, offering pain relief during childbirth or surgery and treating chronic back pain, thus differing in intent and application from LP. The puncture sites for epidural and lumbar puncture are different, however they are procedurally very similar.

The studies cited in [19], such as the one from the 2010 National Inpatient Sample (NIS) and National Emergency Department Survey (NEDS), indicate that annually, in the USA alone, there were approximately 362,718 LPs performed across various age groups in 2010. Notably, radiologists are the predominant practitioners, executing nearly half of these procedures, followed by emergency physicians and neurologists [10].

Despite its routine nature, the LP and epidural processes face significant challenges, particularly in achieving successful anesthesia or analgesia, with failure rates reaching up to 30% [9]. Complications often arise due to the intricate nature of the puncture

sites, where limited visibility and space constraints can cause the risk of inaccurate needle placement. This issue is compounded in patients with varying habitus, where the anatomical landmarks are obscured or atypical, making the procedure more complex and prone to errors.

While ultrasound can serve as a visualization tool for the process, it only helps in seeing the rough bone edges. The interspinous spaces, puncture sites are often obscured due to the shadows from the bones. Our work proposes the integration of 2D ultrasound imaging with 3D MRI model, aiming to create a visualization tool for the lumbar spine and entry locations which might help in bringing ease to the puncture procedure. The real-time, accessible nature of ultrasound with the detail of MRI can help to refine the guidance process for lumbar puncture and epidural procedures.

1.1   Background

The lumbar spine, comprising the lower five vertebrae (L1-L5), is a part of the human vertebral column designed to bear significant body weight and enable flexible movement. In the lumbar region, shown in Figure 1.1, the spinous processes are prominent bony projections that align vertically and are separated by the interspinous spaces, filled with interspinous ligaments and muscles. These spaces are critical for needle passage in procedures like lumbar punctures. Just deep to this area lies the epidural space, an anatomical cavity outside the dura mater containing fat and small blood vessels, frequently targeted for epidural anesthesia. The cerebrospinal fluid (CSF) surrounds the spinal cord within the dural sac, a vital area accessed during lumbar punctures to diagnose or treat neurological conditions.

Lumbar Puncture has become a regular process in which the doctors rely on manual alignment of the needle into the desired location. For accurate diagnostic Lumbar Puncture, targeting the L3/4 interspinal space is recommended [8], [4]. The spinal cord
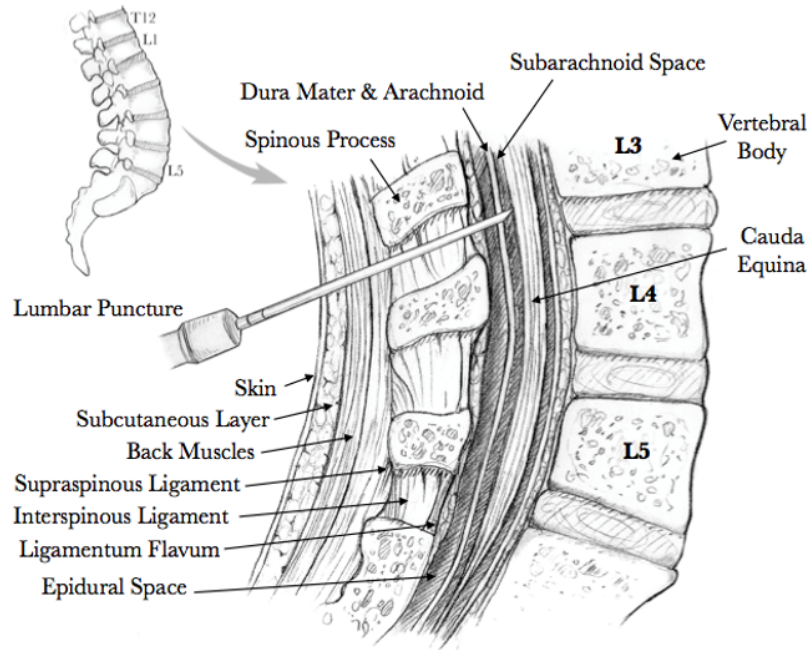
Fig. 1.1 Ligaments of the lumbar spine. Reproduced from [6]

terminates at the level of L1-L2 leaving the fluid-filled lumbar-cistern at L3-L4. The needle is inserted between two spinous processed, in the interspinal space. The distance between the spinous processes tends to increase from the upper to the lower lumbar vertebrae due to the natural curvature and anatomy of the spine. This interspinal spacing can typically range from about 1 to 3 centimeters (cm). Practitioners rely on the bony landmarks of the L4 spinous process, complemented by proprioception during needle insertion, ensuring precise and effective procedure execution. After penetrating the skin tissue, the needle passes through the supraspinous ligament, interspinal ligament, and ligamentum flavum. When the needle tip touches the dura mater outside the arachnoid membrane, the operator should feel a sudden resistance. Overcoming this resistance indicates that the needle tip has reached the subarachnoid space between the arachnoid and pia mater, where CSF can be sampled. An anatomical

review of a clinical lumbar puncture is detailed in [3], with reference to lumbar anatomy illustrated in Fig. 1.2 and Fig. 1.3.
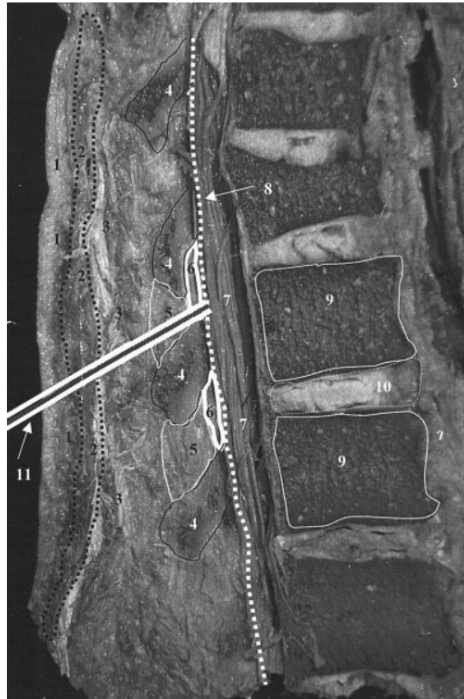
Fig. 1.2 Sagittal section of lumbar vertebrae illustrating the course of the lumbar puncture needle through skin (1), subcutaneous tissue(2), supraspinous ligament (3), interspinous ligament (5) between the spinous processes (4), ligamentum flavum (6), dura mater (8), into thesubarachnoid space and between the nerve roots of the cauda equina(7). Lumbar vertebral bodies (9), intervertebral disc (10), and lumbar puncture needle (11). Reproduced from [3]

1.2   Ultrasound Guided Lumbar Punctures

Ultrasound-guided lumbar puncture is a technique that offers a real-time, non-ionizing, and patient-friendly approach to spinal interventions. Unlike fluoroscopically guided LP, which relies on ionizing radiation, ultrasound guidance utilizes sound waves to create images of the soft tissues in the lumbar region, including the dura mater and surrounding structures. In a teaching setting, ultrasound guidance has been shown to reduce pain and procedure time of LP [13]. Ultrasound primarily serves as a visual aid,
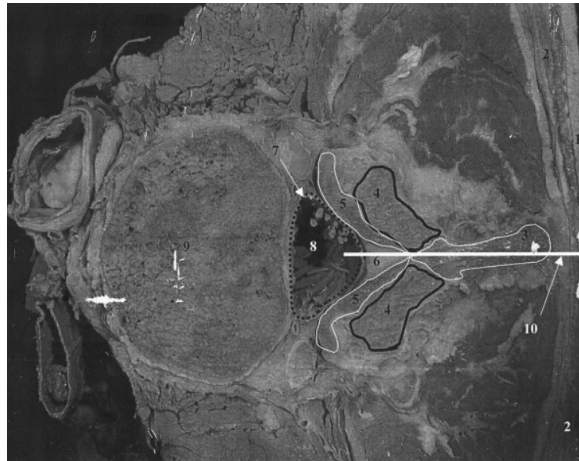
Fig. 1.3 Horizontal section of lumbar vertebra illustrating the course of the lumbar puncture needle through skin (1), subcutaneoustissue (2), between the spinous processes (3) and laminae (4), liga-mentum flavum (5), epidural space(6), dura mater (7), into the subarachnoid space and between the nerve roots of the cauda equina (8).Lumbar vertebral body (9) and lumbar puncture needle (10). Reproduced from [3]

while the actual insertion and alignment of the needle remain manual tasks, dependent on the practitioner's skill and experience. This reliance on manual dexterity means that there is still a margin for error, particularly in challenging cases or with less experienced operators. Additionally, there is a need to localize the needle with respect to the ultrasound probe while the procedure is carried out.

To further increase the accuracy and safety of LPs, research into automated or semi-automated needle guidance systems is ongoing. These systems aim to integrate ultrasound imaging with robotic assistance, allowing for precise needle placement with minimal human error.

1.3   Issues with Lumbar Puncture

Misalignment in such a process require the needle to be pulled out and reinserted. In a study conducted from September 2015 to December 2020 of 844 unique patients , about 77% of lumbar puncture procedures were successful with just 1 to 3 attempts

at inserting the needle, while unsuccessful attempts usually required 3 to 5 insertions to achieve success [16]. This not only makes the procedure longer but can also be uncomfortable and risky for patients due to potential complications. These complications include headaches, cranial neuropathies, prolonged backache, nerve root injury, and meningitis[7]. Thus, while lumbar puncture is considered a routine procedure, its manual execution leaves room for improvement towards associated risks and enhance patient safety. Variations in spine curvature, such as lordosis (inward curvature) or scoliosis (lateral curvature), can alter the typical landmarks used for needle insertion, complicating the identification of the optimal entry point and trajectory. Additionally, obesity can obscure these landmarks further and increase the depth the needle must traverse to reach the subarachnoid space, thus complicating the procedure. Previous spinal surgeries can also present challenges, as scar tissue and anatomical changes may distort the usual landmarks and spaces, leading to a higher risk of failed attempts and needle misplacement. Moreover, as indicated in a study in [14], even with didactic sessions, hands-on training, and three proctored examinations, nineteen attempts were deemed insufficient for fellows to attain proficiency in US-guided LP procedures.

1.4 Literature Review

Several studies have explored innovative approaches in ultrasound interpretation of spinal imaging to address the complexity of lumbar puncture and enhance procedural efficacy. Ultrasound-guided needle guides, allow the practitioner to visualize the needle's path in real-time, ensuring more accurate placement into the subarachnoid space. As the needle is inserted and advanced towards the spinal canal, the ultrasound probe can be positioned to keep the needle in view throughout its trajectory. The authors in [11] proposed an innovative algorithm to generate panoramic spinal images, labeling vertebrae during ultrasound scans. The integrated panorama scale aids in

determining the chosen inter-vertebral space, like L3–4, guiding precise skin marking for efficient localization. Another strategy in [20] employs a support vector machine (SVM) classification algorithm to classify the bone images and interspinous images. The algorithm proposed in [1] registers ultrasound and labeled X-ray images and creates a similarity matrix by pairing spinous process contours. The registration of ultrasound with neuraxial anatomy ground truth, involving the identification of vertebral levels and the spine mid-line, is explored in [17]. Though they work towards spinal imaging and classification, none of them provide labeled data for valid needle insertion regions. A robotic system in [12] introduces a needle manipulator with force feedback, automating needle insertion processes during lumbar puncture. In [5], lockable, articulating needle guide that attaches to an ultrasound probe is proposed. An user-interface is built that provides real-time visualization of the predicted needle trajectory overlaid on the ultrasound image. However, both the papers do not provide a localization of valid needle insertion region.

1.5   Problem Statement and Contributions

We believe that effective visualization can simplify the learning process and enhance the workflow in lumbar puncture and epidural procedures. Our approach leverages 2D ultrasound images, integrating them with a 3D MRI model to define a safe region for needle insertion, thereby aiding practitioners in executing these procedures.

Our work is a step towards improved guidance for ultrasound procedures through better visualization of valid trajectories. Merging simulation, image processing, and MRI ground truth refinement, our solution can aid in the accuracy and safety of lumbar puncture procedures within a simulated environment. The future avenues for this research can focus on developing needle trajectory, alignment, and insertion to achieve automated lumbar puncture.

Chapter 2

Data Collection

2.1 Introduction

In our study, we focused on using ultrasound imaging to help in guidance for lumbar puncture process. We created a 3D point cloud of the lumbar vertebrae of a lumbar spine phantom by using a tracking system with ultrasound images. These images were captured using an ultrasound machine probe and synchronized with the positioning data from the Vicon motion capture system, which forms the basis of our data collection. The ultrasound provided views of the internal structures of a lumbar puncture training model, and the Vicon system helped track where the ultrasound probe was in space. We captured image and tracking information in a single python script, making sure our physical and image data was time-matched. Additionally, to have a reference of reliable anatomy, we obtained MRI scans of the lumbar spine phantom. This MRI provided a definitive anatomical map, serving as the ground truth for registering the obtained ultrasound point cloud.

2.2 Material and Devices

1. GE Logiq E9 Ultrasound Machine

   This versatile and general ultrasound imaging system was used for its real-time imaging capabilities that are essential for guiding the needle insertion process, providing immediate visual feedback. It has adjustable settings specifically for the depth of view and brightness of the images.

2. GE9L Linear Array Ultrasound Probe

   This probe, when used with the GE Logiq E9 machine, specializes in deep tissue imaging, offering images of the lumbar region. It has a frequency range of 3-8 MHz, while the contact ares with the body is 14 x 53 mm. The probe produces linear scans, which are clinically used for lumbar puncture process.

3. DVI to HDMI cable and HDMI to USB video capture card (Magwell, Nanjing, China)

   To capture images in real-time from the ultrasound system, we used a frame capture device connected to the DVI output of the ultrasound system. This method of screen capturing provided an ease in data collection over real time transfer of raw image files..

4. The Phantom: Ultrasound Lumbar Puncture Simulator IIA (Kyoto Kagaku)

   A model that mimics human anatomy of the lumbar spine, to facilitate realistic training and experimental testing using ultrasound imaging. It features a central spinal block made of hard resin, simulating the vertebral structure, and is encased in a soft resin that mimics the feel and appearance of skin and surrounding tissues.

5. Vicon Vantage V5 Motion Capture System

   A motion tracking Vicon system setup was used that provides high-precision

spatial data using 10 mounted cameras. In the context of my research, it's used to track the movement of the ultrasound probe in three dimensions, allowing for the accurate correlation of physical probe location with the virtual imagery obtained during the procedure. We used Vicon Tracker 3.7 API to get spacial data of probe and a registration method between the phantom's anatomical space and the ultrasound imaging space.

6. 3T Clinical MRI (GE Signa Premiere, GE Healthcare, Chicago, Illinois, USA)
   In my study, MRI images serve as the standard for verifying the anatomical accuracy of ultrasound-guided needle trajectories. The high-resolution, three-dimensional images produced by this MRI system are used for creating a detailed anatomical framework against which the ultrasound-guided procedures can be calibrated and improved.

2.3   Ultrasound Image Data

The collection of ultrasound image data was a process, aimed at capturing gross anatomical features of lumbar spine's anatomy that could be used to map edges and generate a sparse 3D point cloud. The screen output of the ultrasound machine was captured at a rate of 0.5 frames per second using video capture card specified in Section **??** using ViconDataStream library in Python, effectively grabbing a frame every two seconds. This method allowed us to obtain a discrete set of images at different locations along the spine. Figure 2.1 illustrates an ultrasound screen capture taken when the probe was aligned along the spinal axis of the Lumbar Puncture Simulator, specifically between the L2 and L3 vertebrae.

Adjustments to the ultrasound machine settings, specifically depth and gain (Gn), play a great role in visualizing the image quality for detailed anatomical analysis.
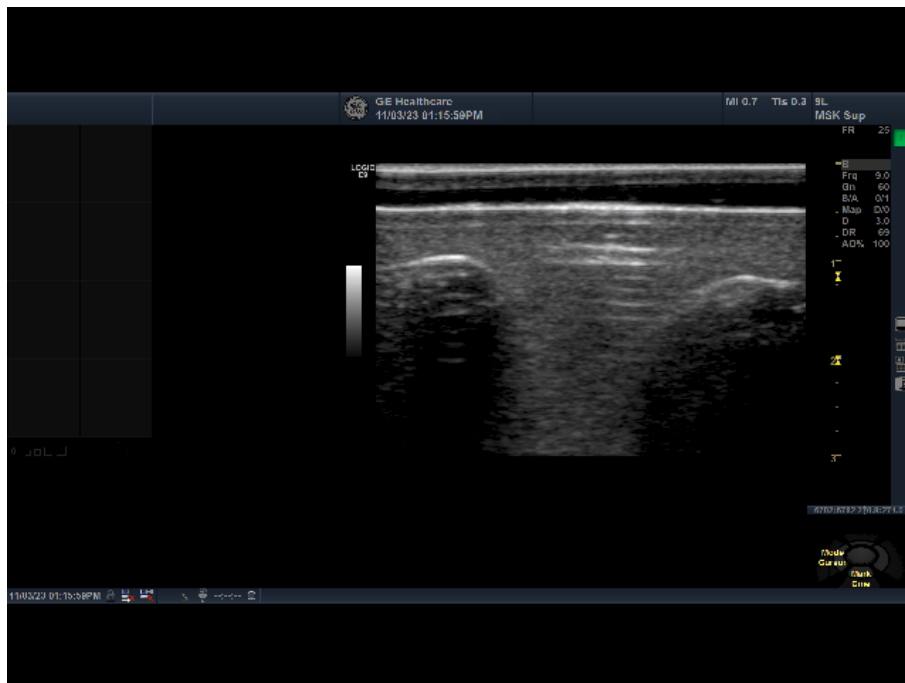
Fig. 2.1 Ultrasound Screen Output when probe is placed between L2 and L3

The depth setting determines how deep the ultrasound waves penetrate into the body. Adjusting this setting allows us to focus on the relevant anatomical structures of the lumbar spine, ensuring that the images capture the required details. Increasing the depth provides a more comprehensive view of deeper structures, while decreasing the depth focuses on the superficial layers, enhancing the clarity of the images in these regions.

The gain setting, on the other hand, affects the brightness and contrast of the ultrasound images. By fine-tuning the gain, we can enhance or reduce the echogenicity (the ability of tissues to reflect ultrasound waves) of the image, making the anatomical landmarks more distinct. Higher gain settings increase the echogenicity, making the image brighter and more detailed, which is crucial for identifying specific anatomical features like the spinous processes and intervertebral spaces. Conversely, lower gain settings reduce the echogenicity, which can help in minimizing the appearance of artifacts and improving the overall clarity of the image.

(a) Gain = 50   (b) Gain = 60   (c) Gain = 70
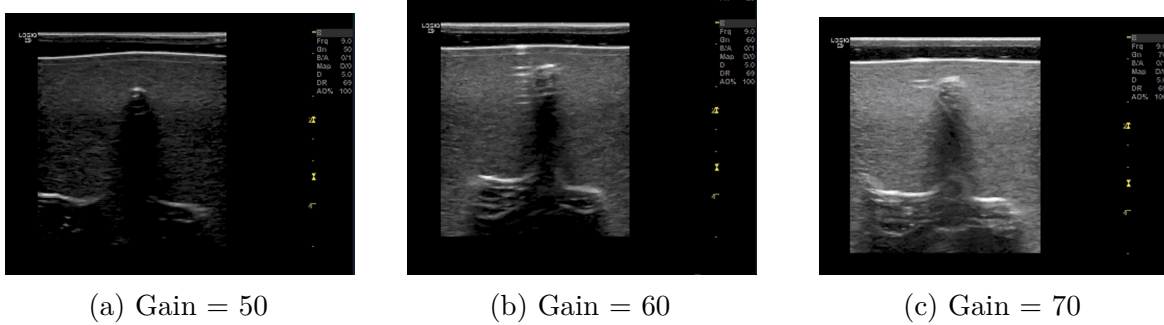
Fig. 2.2 Changing Gain Values With Constant Depth 5 inches

(a) Depth = 4 inches   (b) Depth = 5 inches   (c) Depth = 6 inches
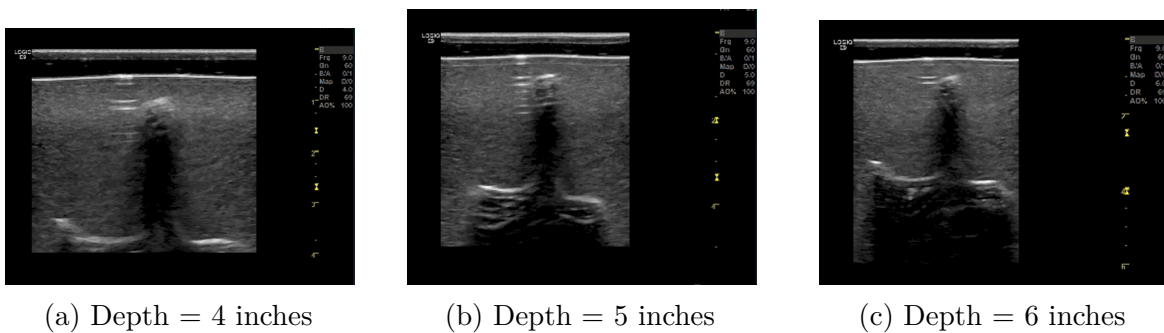
Fig. 2.3 Changing Depth with Constant Gain Value 60

Throughout the data collection process, we experimented with various depth and gain settings to determine the optimal configuration for visualizing the lumbar spine's anatomy. This experimentation allowed us to achieve the best balance between image depth and clarity, ensuring that the ultrasound images provide a reliable and accurate guide for the lumbar puncture procedures. The results of the ultrasound images with different gain and depth values are shown in Fig 2.2 and 2.3.

2.3.1 Ultrasound Probe Placement and View

Proper probe placement is crucial for obtaining informative ultrasound images that accurately reflect the spinal anatomy. The probe's orientation and location determine the anatomical features of the spine visualized and are key to guiding lumbar puncture procedures.

We experimented with two distinct probe placements to identify the best approach for visualizing the lumbar spine:

1. **Vertical Placement of Probe:** Positioning the probe vertically along the mid-line of the lower back allowed us to visualize the spinous processes in detail. The exact view depended on the probe's alignment with specific lumbar vertebrae. This orientation highlighted the spinous processes, presenting them in a clear, 'dome' shape due to the bone's high ultrasound reflectivity.

2. **Horizontal Placement of Probe:** When the probe was placed horizontally, it captured the lateral aspects of the spine, specifically the edges of the superior articular processes adjacent (on both sides) of the spinous processes. This view was particularly useful for understanding the spatial relationship between these bony landmarks.

Figure 2.4 displays the images resulting from these probe placements, with each view capturing different anatomical features. The "dome"-shaped appearance of the spinous processes is seen under vertical orientation and the imaging of the articular processes in the horizontal view. The acoustic shadowing beneath these bone structures indicates region where bones are present.

The sparse 3D point cloud generated from the image and probe-pose data was registered to a ground truth preoperative MRI point cloud. In our study, horizontal orientation of probe was preferred for the registration phase since the image revealed additional landmarks such as the superior articular processes alongside the spinous process. For dynamic lumbar puncture visualization phase, where the primary goal is to clearly view the interspinal gap, vertical probe placement was favored. Furthermore, the depth setting was adjusted to 5 inches, and the gain (Gn) was set to a value of 60. These parameters were determined through experimentation to identify the settings that most complemented our edge detection algorithm.

(a) Image Obtained

Spinous Process Tip

Acoustic Shadow
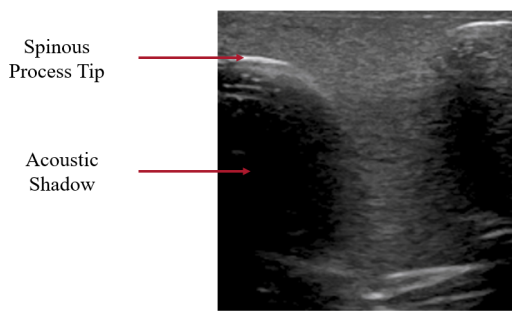
(b) Placement of Probe (Vertical)

(c) Image Obtained

Spinous Process Tip

Acoustic Shadow

Articular Process Tip
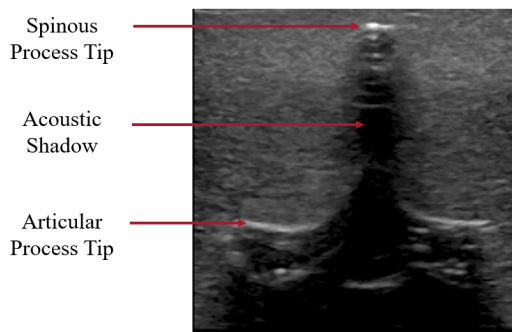
(d) Placement of Probe (Horizontal)

Fig. 2.4 Ultrasound Probe Placement and View

2.4   Probe Pose Data

The ultrasound probe used in our study was customized with a Vicon marker cuff, illustrated in Figure 2.5. This cuff was outfitted with three markers, positioned for integration with the Vicon motion capture system. These markers facilitated the real-time tracking of the ultrasound probe's spatial orientation, making it possible to monitor its exact position during image acquisition.

The probe covers were designed with a cavity feature to ensure fit and alignment to the probe. These covers were crafted in two halves, which were then joined using fasteners. This design gave a snug fit around the ultrasound probe and allowed for the placement of Vicon markers at the designed locations for motion tracking.

The markers were placed in three different directions around the probe, each at slightly varying heights to provide a varied spatial reading. This enabled the Vicon motion capture system to track the probe's position and orientation with high precision.

Each marker acted as a fiducial point for capturing the probe's pose accurately at every moment an ultrasound image was taken. The spatial data for all three markers were continuously recorded in relation to a predefined world-coordinate system, and then were time-synchronized with the ultrasound imaging events. The synchronization of the image and Vicon data streams, which operate at different speeds, was achieved through a custom Python script. This script ensured that with each capture of an image, the most recent Vicon data was also recorded. The script interfaced with the Vicon Tracker API using the ViconDataStream library, enabling the simultaneous collection of images and corresponding marker poses. The data for images were saved in a folder and its respective marker poses were compiled into a .csv file for each dataset. The flowchart for the synchronization is shown in Figure 2.6. This synchronization between the ultrasound image acquisition and the pose data collection built a combined in-sync image-probe pose dataset.
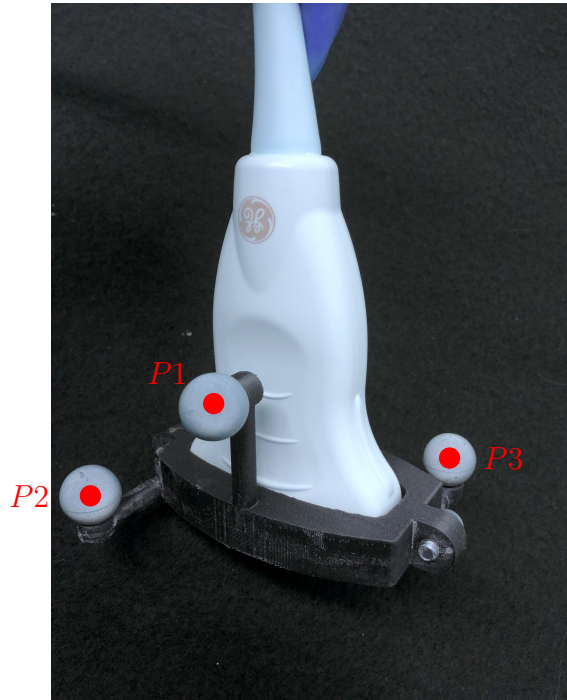
Fig. 2.5 Ultrasound Cuff with Markers (P1, P2, P3)

The combination of these datasets—ultrasound images and corresponding spatial orientation data—allowed for the construction of a detailed point-cloud representation of the lumbar vertebrae. By merging the two-dimensional ultrasound images with the three-dimensional positional data from the Vicon system, we were able to reconstruct the lumbar spine's anatomical features in a three-dimensional space.

2.5   MRI Ground Truth Data

To establish a ground truth model of the lumbar phantom, essential for visualizing the anatomical structures and potential needle entry points, we initiated a process to create a 3D mesh representation using Magnetic Resonance Imaging (MRI). These scans were captured in DICOM format, providing the detailed data necessary for 3D modeling.
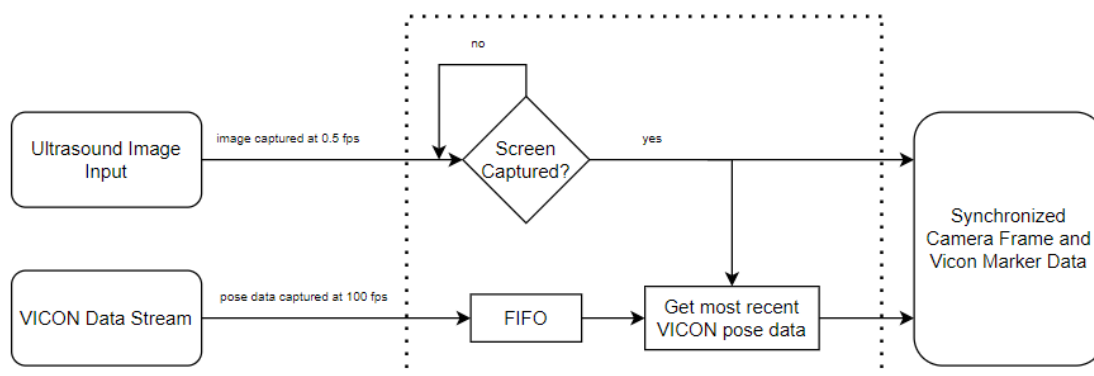
Fig. 2.6 Flowchart for Camera-Vicon Time Synchronous Data Collection

The voxel size for the MRI scan was selected to be 0.293mm x 0.293mm x 1.000mm, amounting to a volume of approximately 0.085849 cubic millimeters. The use of a 3D T1-weighted BRAVO sequence, complemented the voxel dimensions, formed the visualization of the lumbar spine structures. These specifications provided the data for constructing an accurate 3D mesh of the lumbar phantom while keeping the scan duration within practical limits.

The series of scans in the DICOM format achieved from the MRI process were converted to solid mesh using the software Slicer 5.4.0. The Volume Rendering model in Slicer converted the 2D sliced to a 3D model, and Segmentation and Threshold model helped to alienate the lumbar vertebra from the background. The noise data was removed using the Island and Scissor tools. By exporting the model a .STL file of the model, the 3D mesh was achieved. A screenshot of the slicer software interface with the stacked slices and rendered 3D model is illustrated in Fig 2.7.

The STL file achieved from Slicer was then converted into a point cloud (PCD) file using Open3D point cloud library. The point cloud, shown in Fig 2.8, is the ground truth for aligning and registering ultrasound-generated point clouds, to achieve anatomical reconstruction between the two modalities.
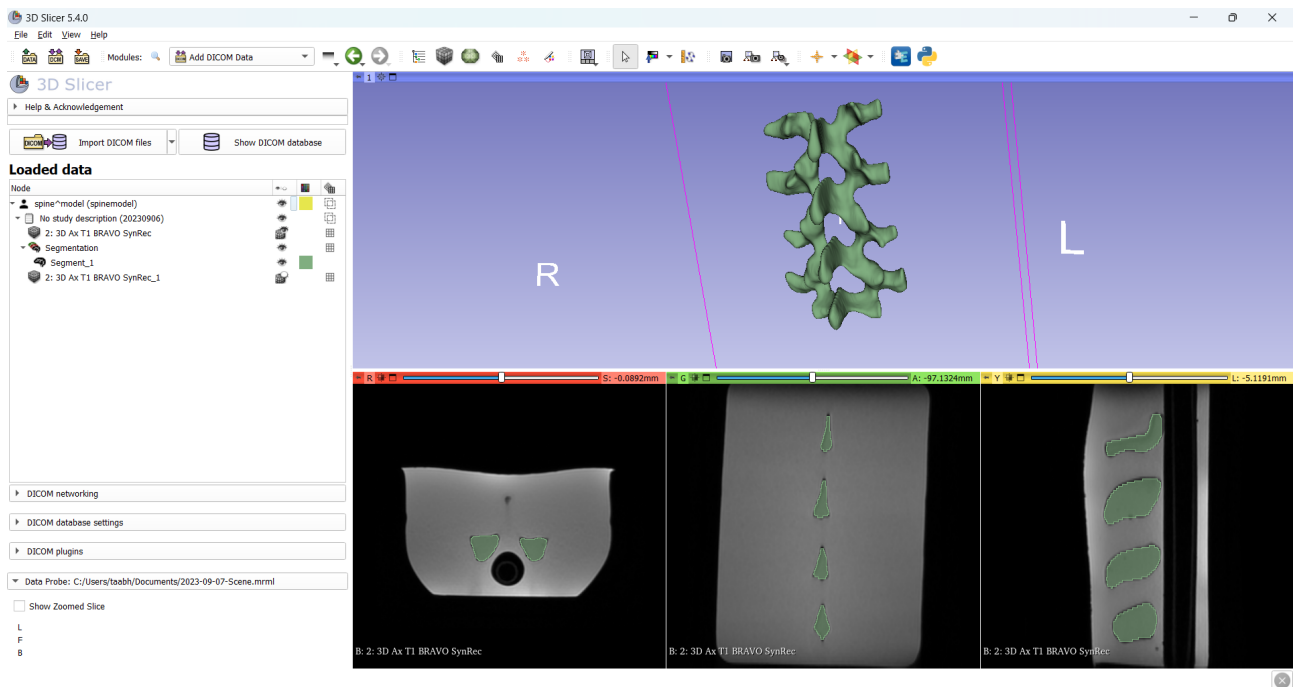
Fig. 2.7 Screenshot of the Slicer Interface with the Stacked Slices and Rendered 3D model

(a) Front View   (b) Side View
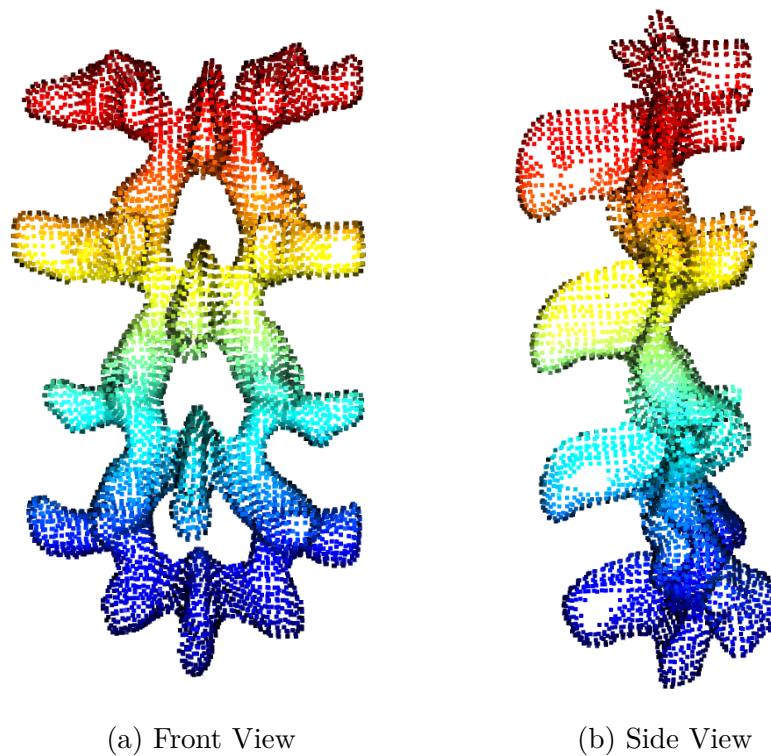
Fig. 2.8 MRI Ground Truth Point Cloud

Chapter 3

Methodology

The methodology comprised of an ultrasound image processing technique, including a edge-detection method tailored for determining the edges of spinous processes in the images. We performed the construction and calibration of an ultrasound-derived point cloud, which was registered against MRI data. This allowed for the overlay of MRI-identified safe insertion regions onto ultrasound imagery. Through iterative refinement and local optimization, we formed a framework that forms a visualization tool for lumbar puncture procedures.

3.1   Ultrasound Image Processing

In our ultrasound image processing, we aimed to identify the outline of lumbar bone structures within the ultrasound images. As depicted in Figure 2.1, the ultrasound imaging captured the entire screen, including the lumbar bones visible as bright white spots at the top, forming a distinctive "dome" shape.

The images were initially processed by cropping to isolate the lumbar bone region, eliminating unnecessary details such as the skin lines that did not contribute to
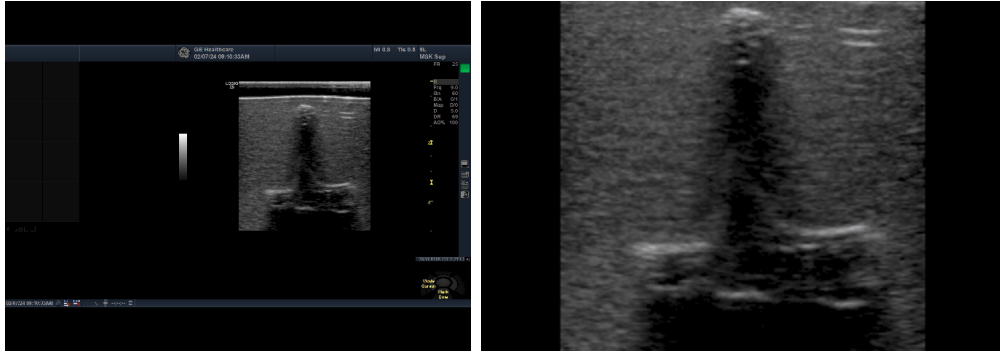
(a) Original Capture of Ultrasound
Screen

(b) Cropped Image used for Our Method-
ology

Fig. 3.1 Cropping of Ultrasound Images

identifying the lumbar bone edges. An example of a cropped image focusing on the
lumbar bone is shown in Figure 4.3.

3.1.1 Literature

A series of researches worked with feature extraction and identification in a lumbar
ultrasound. The algorithm in [18] utilizes phase symmetry to highlight features in
ultrasound images, aiding in the detection of bone (lamina) and ligamentum flavum
(LF). It combines phase symmetry with Gaussian and Log-Gabor filters to generate a
detailed ridge map, then applies Pearson's cross-correlation for template matching to
accurately locate the lamina and LF within the image.. The method in [15] utilizes
local phase-symmetry to enhance bone-like structures in the images, aiding in the
accurate identification and classification of spinal elements (spine blobs). In [2], a deep
convolutional neural network U-net architecture, is employed for bone segmentation
from ultrasound imaging. This method involves matching the shapes of spinous
processes predetermined from a lateral X-ray with those segmented in real-time 2D
sagittal ultrasound images. The system optimizes the segmentation process to align

the mean of the X-ray contour with the center of mass of the detected bones in the ultrasound image.

For building a 3D point cloud in our study, we needed an algorithm to track as much of the bone edge as possible. We employed a non-expensive classical computer vision algorithm for tracking the spinous process tip, its edge, as well as articular process tip in an ultrasound image captured by horizontal placement of probe.

3.1.2   Goal of Edge Detection

Our image processing approach aimed to delineate the lumbar bone edges in the images. In these ultrasound images, we targeted three main features:

- **White Domes:** These are indicative of the bone tips, appearing as bright white due to their high echogenicity.

- **Black Shadows:** Caused by ultrasound wave reflection off the bone, this shadow aids in defining the bone edge.

- **Noise:** Present as random granular patterns and spots, complicating the clear identification of anatomical structures.

Initial image processing attempts involved blurring techniques combined with the Canny edge detector or color thresholding methods, as illustrated in Figure 3.2. These techniques, however, faced significant challenges. Image noise and varying image qualities led to the blurring process inadvertently masking crucial details or introducing false edges, thereby complicating the delineation of bone edges.

Given these issues, we formed a hybrid novel approach that combined adaptive filtering to better accommodate the image noise and textural properties. This method allowed for a more accurate and reliable identification of the lumbar spine's structural boundaries.

(a) Thresholding   (b) Canny Edge-Detection   (c) Our Edge-Detection
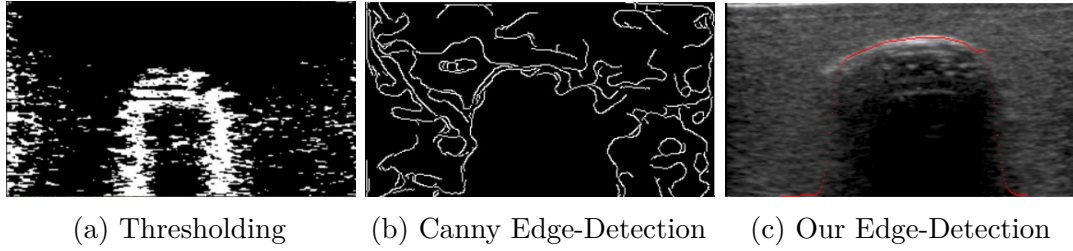
Fig. 3.2 Edge Detection Methods Implemented

3.1.3 Our Edge-Detection Method

Our bone detection methodology is designed to identify the lumbar bones in ultrasound images, with an emphasis on capturing the contours of the spinous process and articular processes present in a given image.

In our refined hybrid approach, each grayscale ultrasound image is analyzed to isolate the highest-intensity regions. These bright spots, exhibiting intensity values surpassing a predefined threshold, typically represent the apex of the lumbar bones. However, given the inherent noise in ultrasound imaging, simply identifying the bright spots is insufficient.

To enhance our detection precision, we incorporated a step to pinpoint "transition points" across the image based on the distribution of intensity values. By scanning each column of the grayscale image, we monitored the intensity variations along the rows. A characteristic pattern was observed in bone-containing regions: a gradient transition from the lower-intensity signals at the top (attributable to surrounding soft tissues) to pronounced darkness towards the bottom, indicating the bone's acoustic shadow. These areas displayed notable intensity jumps, marking the transition from bone to non-bone tissue. In the implemented algorithm, a loop iteratively evaluates each pixel along a specified row by cumulatively summing the pixel intensities. For each pixel considered, the algorithm calculates the average intensity of the pixels above (i.e., preceding pixels in the sequence) and compares it to the average intensity of
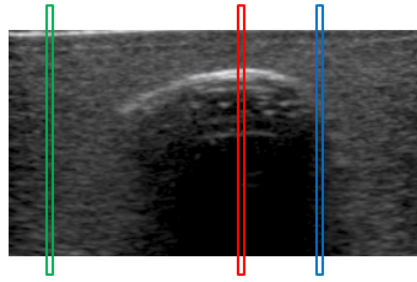
Fig. 3.3 Three Columns Selected and Highlighted in an Ultrasound Image
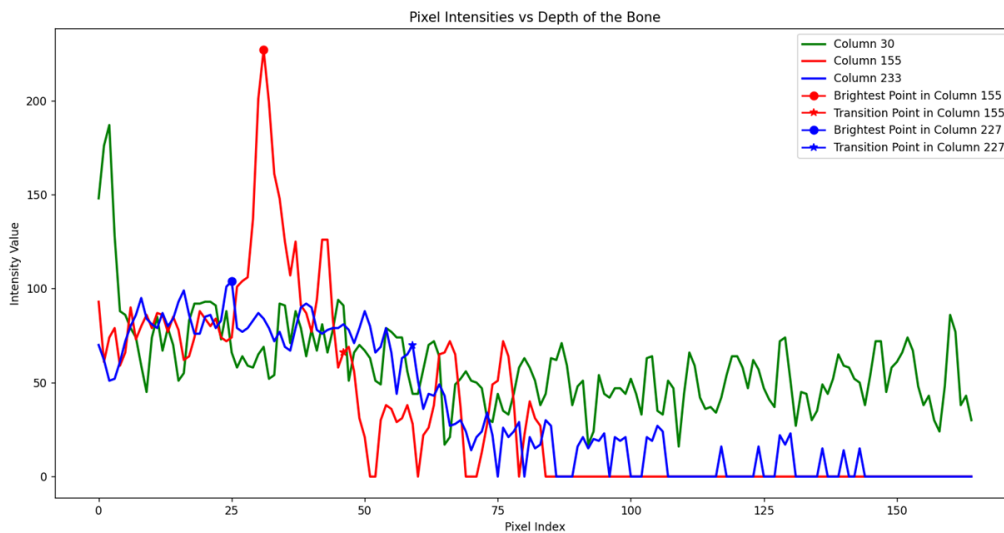
Fig. 3.4 Corresponding Intensity Signals for the Columns in Fig 3.3

the pixels below (i.e., subsequent pixels in the sequence). A pixel is designated as a 'transition point' if the difference between these two averages exceeds a predetermined threshold, here set to 40.

The identified transition points, where significant intensity changes occurred, were mapped out as the bone edges. By selecting relevant points among the bright and transition areas, we were able to construct a detailed edge map of the bones. This process culminated in a clear delineation of the bone contours, enhancing the accuracy of the lumbar puncture guidance.

Figure 3.4 shows the intensity signals achieved from three different columns in a typical lumbar ultrasound image.
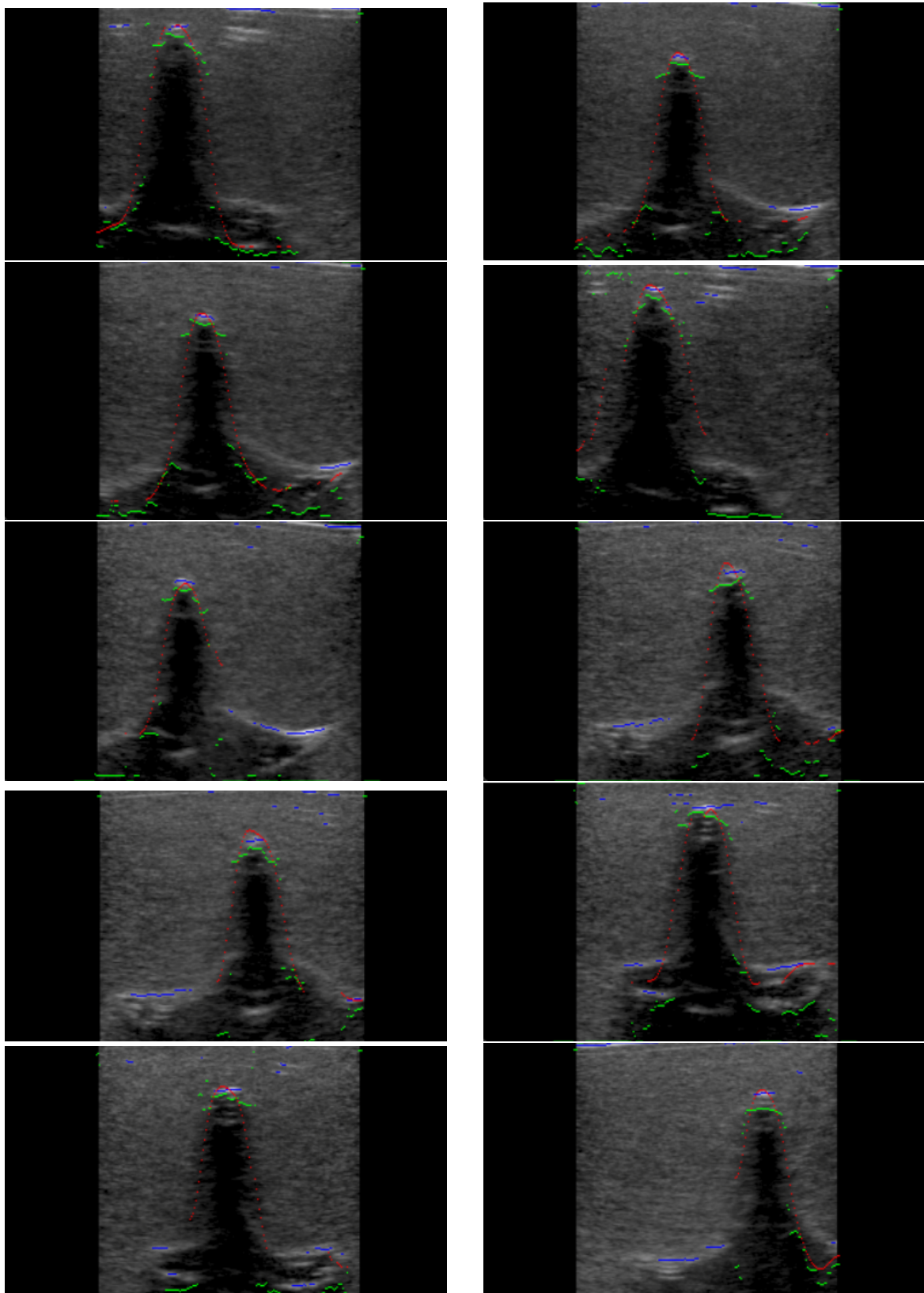
Fig. 3.5 Edge Points Using Transition Points Method: (a)blue=brightest points (b)green=transition points (c)red:selected edge points

In our visualization, we use a color-coding scheme to differentiate between various key features in the ultrasound images. The brightest spots within the image, indicative of the bone apexes, are marked with blue points. These points highlight areas of highest echogenicity, which are critical for identifying the bone's topographical features.

The green points represent the transition regions in the image. These are areas where there is a significant shift in intensity, typically marking the boundaries between soft tissue and bone or the edge of the bone itself. These transition regions are essential for understanding the bone's contour and its interface with surrounding tissues.

Finally, edge points (marked in red) are selected by evaluating the proximity of the brightest (blue) and transition (green) points. When the distance between the brightest and transition points is less than 50 pixels, the brightest point is designated as the edge point. Conversely, if this distance exceeds 50 pixels, the brightest points are considered as artefacts of noise, and the transition points are then selected as the true edge points. Given the significant noise present in the data, initially identified red points were dispersed, and failed to maintain the shape of the required lumbar bones. To address this, we applied a Gaussian fitting to these scattered points, which showed a closer representation of the bone edges contours. Figure 3.5 showcases the application of this method on several ultrasound images, demonstrating the effective identification of bone edges and the outlining of the spinous process.

3.2   Reconstruction of Ultrasound Point Cloud

The reconstruction process of the ultrasound point cloud was parallel to traditional 3D point-cloud reconstruction methodologies. Edge points identified in the ultrasound images were treated analogously to corner points in standard images, facilitating their use in three-dimensional space reconstruction. The center of the ultrasound probe

served as the equivalent of the camera center, providing a reference point for spatial orientation and mapping.

3.2.1   Ultrasound-to-World Registration

In our work, Vicon frame was considered at the world frame, and the other frames were related to the world frames accordingly.

Ultrasound Probe Co-ordinates

To define the coordinate frames for the ultrasound probe, we established the center of the probe tip as the origin point. The orientation of the ultrasound probe's coordinate system was designed with the Y-axis extending outward from this origin, aligned with the direction of the ultrasound wave propagation. Since Vicon helped to capture the poses of markers as not the probe tip, we defined a system to get the pose of the probe tip using the pose of the markers.

Using CAD model of the probe cuff, we calculated the distances of the markers from the probe tip (origin). The poses of three markers be M1, M2, M3 with measured with respect to origin (probe-tip). The transformation of probe tip with respect to centroid, $^{\text{probetip}}T_{\text{centroid}}$, was determined using the calculations in Section A.0.1.

Probe Prose in World Co-ordinates

During data capture process, The poses of three markers were continuously captured in the world co-ordinate frames using Vicon. These poses were used to calculate pose of marker centroid in world frame using the same calculations in Section A.0.1. Thus, for each image captured, a $^{\text{world}}T_{\text{centroid}}$ was recorded. From this, the pose of probe tip was then calculated using:
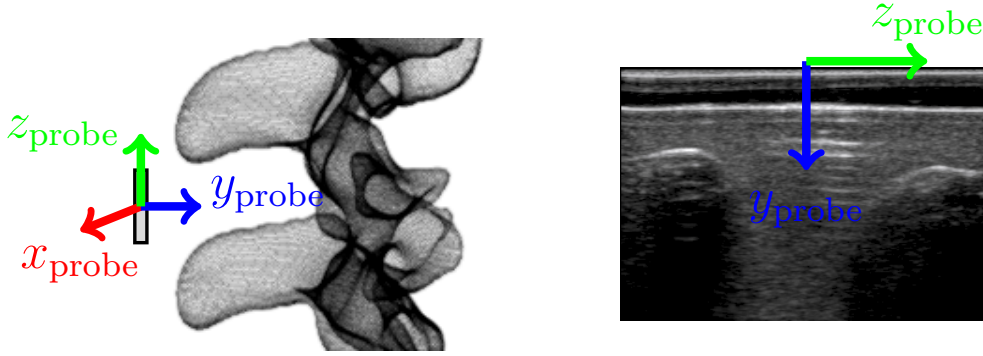
Fig. 3.6 Coordinate Systems for Ultrasound Probe Tip and Images

$$^{\text{world}}T_{\text{probetip}} =^{\text{world}} T_{\text{centroid}} \cdot^{\text{centroid}} T_{\text{probetip}} \tag{3.1}$$

This gave a transformation matrix of probe pose with respect to the world frame. When a series of images were recorded, the transformations for their respective $^{\text{world}}T_{\text{probetip}}$ were also calculated.

Ultrasound Image Co-ordinates

Correspondingly, the ultrasound image frame was oriented to ensure the Y-axis pointed toward the bone structures, maintaining consistency with the probe's directional path. Figure 3.6 visually depicts the given axes from probe and ultrasound image. This facilitated the determination of the transformation between the image and the probe tip.

In the the above case (Fig 3.6), we defined that:

$$^{\text{probetip}}T_{\text{image}} = \begin{bmatrix} 0 & 0 & 1 & 0 \\ 0 & 1 & 0 & -36 \\ -1 & 0 & 0 & imagewidth/2 \\ 0 & 0 & 0 & 1 \end{bmatrix}$$

By establishing the transformation matrices from the ultrasound probe frame to the world frame, and from the ultrasound image frame to the probe frame, a transformation pathway was derived. This culminated in the reconstruction of the ultrasound image frame to the world frame transformation, thus enabling the reconstruction of the ultrasound point cloud in a real-world context.

3.2.2   Building a Point Cloud

For building point cloud from the edge-points calculated in Section 3.1.3, they were transformed from image frame to world frame using $^{\mathrm{world}}T_{\mathrm{image}}$. Thus, for ever pair of edge point in image co-ordinate and the respective $^{\mathrm{world}}T_{\mathrm{probetip}}$ of that image, $^{\mathrm{world}}T_{\mathrm{image}}$ was calculated as follows:

$$^{\mathrm{world}}T_{\mathrm{image}} =^{\mathrm{world}} T_{\mathrm{probetip}} \cdot^{\mathrm{probetip}} T_{\mathrm{image}} \tag{3.2}$$

This $^{\mathrm{world}}T_{\mathrm{image}}$ was used to plot the 2D image edge-points into 3D co-orindate system. Once the edge-points were identified from multiple images and their coordinates were mapped within the world frame, these points constructed a sparse point cloud representing the lumbar vertebrae. Due to the inherent limitations of ultrasound imaging, which typically captures only a segment of the spinous process and articular process, the resulting point cloud primarily delineated these specific spinal structures.

To ensure accurate representation in the point cloud, scaling was applied to the image co-ordinate along with transformation. This was achieved by correlating the dimensions of the ultrasound image (measured in pixels) with the actual field of view and depth (measured in millimeters) of the ultrasound probe. This correlation process involved a comparison between the two-dimensional image scale and the three-dimensional spatial metrics, ensuring that the point cloud accurately reflected the anatomical size and proportions.

(a) Front View   (b) Side View   (c) Orthogonal View
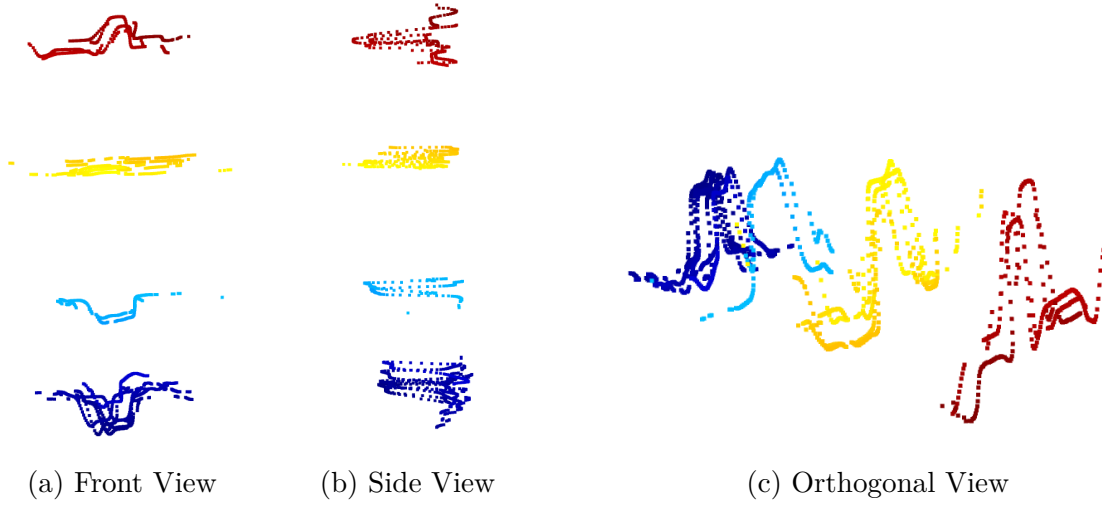
Fig. 3.7 Ultrasound Point Cloud

This scaling process was used for translating the two-dimensional ultrasound image data into a three-dimensional point cloud that represents the lumbar spine's anatomy. It allowed for the calibration of the point cloud against the known dimensions of the lumbar vertebrae. The generated point cloud, as illustrated in Figure 3.7, is in the world co-ordinate system and it provides a detailed and spatial representation of the spinous processes.

3.3   Ultrasound-MRI Point Cloud Registration

The limitation of the ultrasound point cloud's sparsity was that it only partially reveals the bone structure. To overcome this, we aligned the ultrasound-generated sparse point cloud with the more comprehensive MRI-derived ground truth point cloud. This alignment process integrated sparse ultrasound data with the dense MRI point cloud, thereby enriching the visualization of the lumbar spine anatomy.

The Iterative Closest Point (ICP) algorithm, renowned for its point cloud alignment algorithm, was employed to achieve registration between the ultrasound and MRI point clouds and get a $^{\text{US}}T_{\text{MRI}}$ transformation. Utilizing the Open3D library's implementation

of the ICP algorithm, we conducted 3D-3D point cloud registration, refining the alignment by iteratively minimizing the distance between the corresponding points of the two datasets.

3.3.1   Initial Estimate of US-MRI Transformation

A particular aspect of the ICP registration process is the availability of a reliable initial estimate of the transformation matrix. A close initial guess significantly enhances the accuracy and efficiency of the algorithm's convergence. To establish this initial alignment, we devised a method to determine correspondences between the ultrasound and MRI point clouds, based on anatomical landmarks.

During ultrasound data acquisition, the probe was positioned approximately at the center of each lumbar bone (L1-L4) along the mid-line axis. This placement facilitated the identification of key points within the ultrasound images, where the lumbar bones appeared roughly at the image's center. These identified points from the ultrasound data served as source correspondences for the point cloud alignment process.

Correspondingly, in the MRI ground truth data, we identified points that served as virtual probe positions, approximating the centers of the lumbar bones L1-L4. This methodological approach ensured that both point clouds had four corresponding points, representing the central anatomical landmarks of the lumbar vertebrae.

By establishing these 4-to-4 point correspondences, we generated an initial rough transformation matrix $^{\mathrm{US}}T - initial_{\mathrm{MRI}}$, serving as a foundational alignment for the subsequent ICP refinement process.

3.3.2   Iterative Closest Point Algorithm

The initial estimate of the transformation matrix found roughly aligned the source point cloud (ultrasound-generated point cloud) to the target point cloud (MRI-generated

point cloud). Then, we used the ICP algorithm which performed an iterative process, where for each iteration, it performs the following steps:

1. Correspondence Finding: The algorithm identifies pairs of points between the two point clouds that are closest to each other, within a specified maximum distance. This threshold helps in excluding pairs that are too far apart, reducing the impact of outlier matches.

2. Transformation Estimation: Using the identified pairs, the algorithm calculates an optimal transformation (rotation and translation) that minimally adjusts the source point cloud towards the target. This step is achieved using a TransformationEstimationPointToPoint method, which computes the transformation based on minimizing the squared distances between corresponding points.
Let $PCD_{US} = \{us_i\}_{i=1}^{N}$ be the ultrasound source point cloud, while $PCD_{MRI} = \{mri_i\}_{i=1}^{N}$ be the MRI target point cloud.

$$^{US}T_{\mathrm{MRI}} = \underset{T}{\arg\min} \sum_{(mri_i, us_{j(i)}) \in C} \left\| (Rmri_i + t) - us_{j(i)} \right\|^2 \tag{3.3}$$

3. Applying Transformation: The calculated transformation is applied to the source point cloud, bringing it closer to alignment with the target point cloud.

$$us_i' = Rus_i + t, \quad \forall us_i \in PCD_{US} \tag{3.4}$$

4. Convergence Checking: The algorithm evaluates whether the convergence criteria have been met. In our configuration, the convergence is assessed based on the maximum number of iterations. The process stops if the algorithm reaches the maximum number of iterations or other convergence criteria specified within the ICPConvergenceCriteria.

(a) Front View   (b) Side View   (c) Orthogonal View
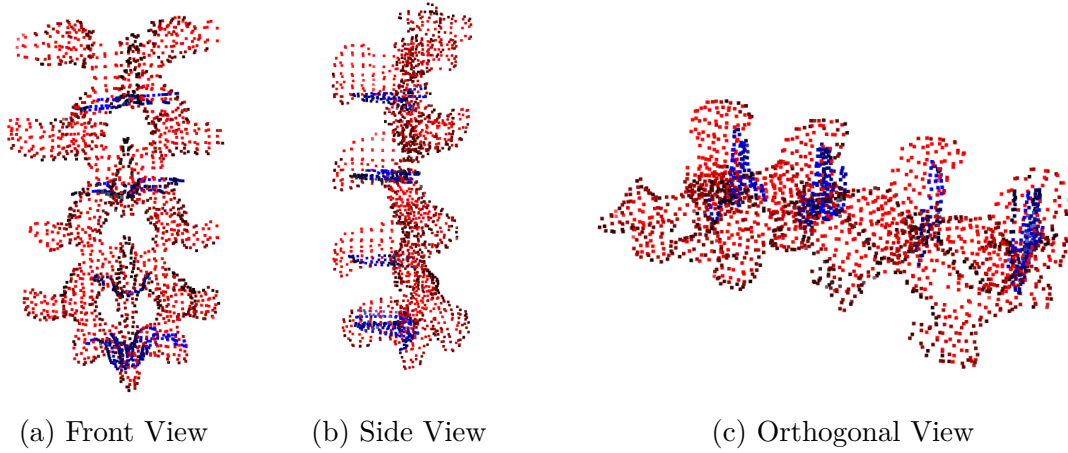
Fig. 3.8 Aligned US-MRI 3D Point Clouds

The result of this iterative process was a refined transformation matrix ${}^{\text{US}}T_{\text{MRI}}$ that closely aligned the ultrasound point cloud to the MRI point cloud, as shown in Fig 3.8. But since ultrasound point cloud was built in the world co-ordinate system, we can say that:

$${}^{\text{US}}T_{\text{MRI}} = {}^{\text{world}}T_{\text{MRI}}$$

Taking into consideration the irregularities in the edge detection process, along with human and body motion, discrepancies in the calculation of ${}^{\text{world}}T_{\text{MRI}}$ are inevitable. The transformation we get from the above calculations were used for dynamic data collection, and they were locally optimized during the process.

3.3.3   Local Optimization of MRI-US Transformation

While the Iterative Closest Point (ICP) algorithm is effective in aligning point clouds, we encountered challenges related to slight movements by the practitioner, the model, or the patient's body, which could affect the accuracy of the spatial positioning. To solve these issues and update the registration at regular intervals, we implemented a local optimization technique that operates subsequent to each dynamic registration event of the image and pose capture.

This optimization process starts with the transformation matrix obtained from the ICP algorithm, denoted as $^{\text{world}}T_{\text{MRI}}$. We use this matrix to dynamically register the current ultrasound image with the corresponding spatial location in the MRI ground truth dataset. Specifically, we transform the current pose of the ultrasound probe into the MRI coordinate system, allowing us to extract an MRI image slice that closely corresponds to the ultrasound image being analyzed.

$$^{\text{MRI}}T_{\text{probepose}} = ^{\text{MRI}}T_{\text{world}} \cdot {}^{\text{world}}T_{\text{probepose}} \tag{3.5}$$

Let 3.9 (a) be the i_{th} ultrasound image captured during dynamic data collection, we can get $^{\text{MRI}}T_{\text{probepose}_i}$ using Equation 3.5. Using this as the probe tip origin, an algorithm was employed which takes a ultrasound equivalent slice of the MRI point cloud from the given probe location. The ultrasound equivalent MRI slice for the i_{th} image is given in Figure 3.9 (b).

To refine the alignment between these two image slices, we employed edge detection techniques as described in Section 3.1.3 on the ultrasound image. This process involves isolating the bone edges in the image. We also obtain the bone edge-points in the corresponding MRI image slice.

Let P_{US} be the set of bone edge points from the ultrasound image, and $\hat{P}_{\text{MRI}}$ be the set of corresponding MRI points using the defined virtual probe. The cost function is defined as:

$$\text{cost} = \frac{1}{N} \sum_{i=1}^{N} \| \hat{P}_{\text{MRI}}^{(i)} - P_{\text{US}}^{(i)} \|^2 \tag{3.6}$$

This cost function minimizes the squared Euclidean distance between corresponding MRI and ultrasound points. By minimizing this cost function, we proceeded to optimize the transformation matrix $^{\text{US}}T_{\text{MRI}}$. This is achieved by aligning the bone edges from the ultrasound image with those from the MRI slice, , illustrated in Figure 3.10,
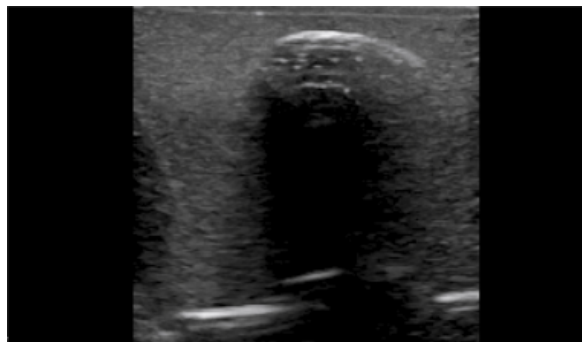
(a) Ultrasound Image

(b) Corresponding MRI Slice to Ultrasound Image

Fig. 3.9 Corresponding MRI Image Slice
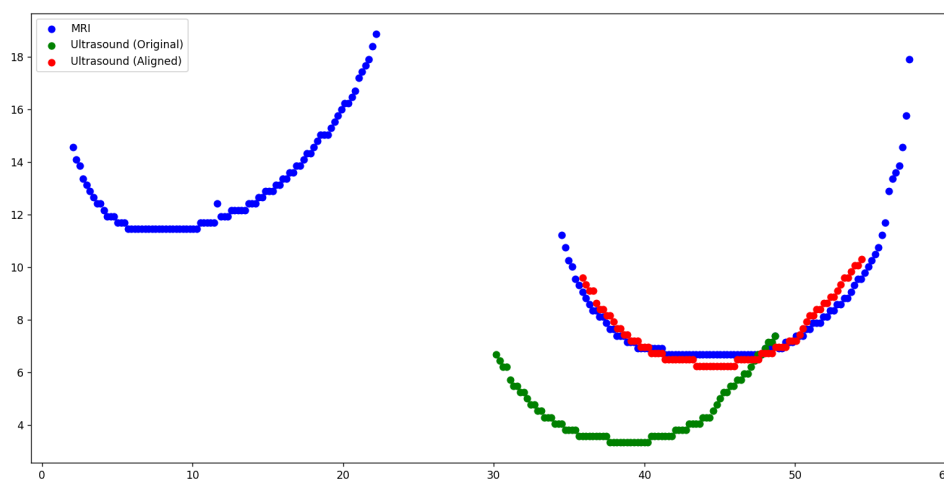
Fig. 3.10 Optimization of Initial Ultrasound Edges (Green) to Aligned Ultrasound Edges (Red) Towards Ground Truth MRI edges (Blue)

ensuring that the anatomical structures are matched across both datasets. This step is compensated for any discrepancies caused by ICP inaccuracy, movement or positional changes during the procedure, thus ensured fine tuning for in the final MRI and probe-tip transformation ($^{\mathrm{MRI}}T_{\mathrm{probepose}}$) and subsequently, an optimized world-MRI registration ($^{\mathrm{world}}T_{\mathrm{US}}$).

Algorithm 1: US-MRI Registration Optimization Algorithm

    Input: Dynamic US images and Vicon-US-probe-poses (x_{us}), T_MRI_US
         from ICP
    Output: Locally Optimized T_MRI_US

1 **for** *each dynamically captured data* **do**
2   Extract bone points in US-image
3   Get MRI-probe-pose from T_MRI_US
4   Get US equivalent MRI slice
5   Extract bone points in MRI image
6   Perform optimization (3.6) between corresponding MRI-probe-pose and
       Vicon-US-probe-pose to locally optimize T_MRI_US

This local optimization process considered that an ultrasound image of the lumbar bone with detected edges is captured. If the captured image cannot determine the edge points, the local optimization did not take place. Instead the $^{\mathrm{world}}T_{\mathrm{US}}$ remained unchanged until next image was captured.

3.4   Safe Region of Needle Insertion

With the establishment of transformations between the MRI and ultrasound (US) data, and between these modalities and the world frame, we have facilitated the accurate identification and mapping of safe regions for needle insertion within the ultrasound images.
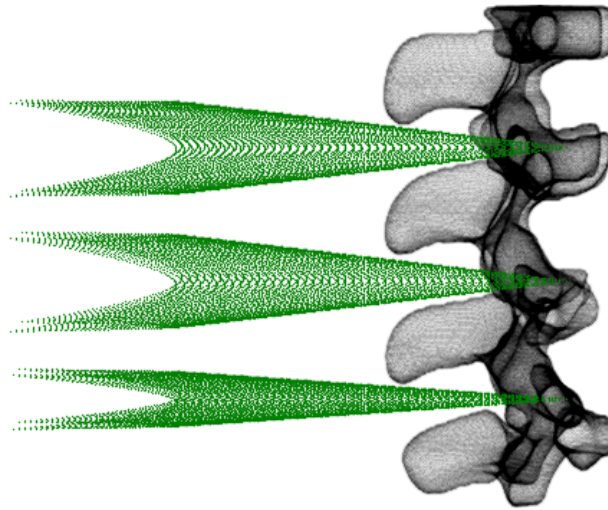
Fig. 3.11 Safe Region Cone from MRI Ground Truth

3.4.1 Definition of Region of Safe Insertion

Considering the MRI data as the definitive ground truth for anatomical structure, regions identified as safe for needle insertion in the MRI are designated as the global safe zones. A possible region for safe needle insertion as "cones," illustrated in Figure 3.11 was conceptualized. These cones originate from manually chosen insertion points and extend outward from the body, ensuring avoidance of bone structures. These cones are not rigidly fixed; they are designed to be adaptable, allowing for adjustments based on individual patient anatomy, practitioner preference, or specific clinical scenarios. This flexibility ensures that the safe insertion regions can be customized for optimal clinical outcomes.

3.4.2   Overlaying the Safe Region on Ultrasound Data

The integration process involves mapping the safe region cones, defined in the MRI point cloud, onto the corresponding ultrasound image space. This is accomplished through the application of the transformation matrices that link the ultrasound image frame with the MRI ground truth data.

When these cone points are transformed into the ultrasound image space, they delineate a shaded area on the ultrasound image, known as the "Safe Needle Insertion Region." This region indicates where the needle can be inserted without risk of encountering bone or other critical structures. An overview of the process is given in Algorithm 2.

Algorithm 2: Realtime Registration and Safe Region Generation

---
Input: Safe Insertion MRI Point Cloud, US-image with Vicon-US-probe-pose, most recent T_MRI_US
Output: Safe Region Overlayed US-image
1 Use US-probe pose and T_MRI_US to get MRI slice
2 Extract bone points from MRI slice
3 Extract bone points in US-image
4 Optimize to calculate $T\_MRI\_US\_new$
5 Use $T\_MRI\_US\_new$ to get Safe Insertion MRI slice
6 Overlay the safe region on US image

This overlay process not only visualizes the safe pathways for needle insertion in the context of real-time ultrasound imaging but also enhances the guidance for practitioners during procedures. The results and implications of this method are elaborated further in Section 4.

An example result for mapping of the safe needle insertion area onto the ground truth are shown in Figure 3.12.
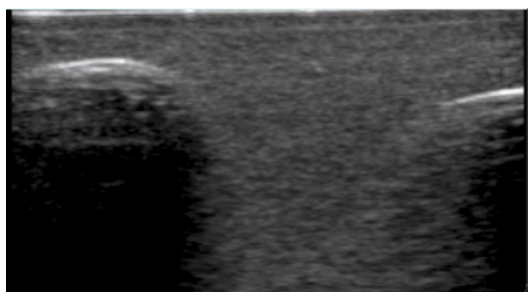
(a) An Input Ultrasound Image

(b) Safe Area (in green) Overlayed with an Image Slice from MRI Ground Truth
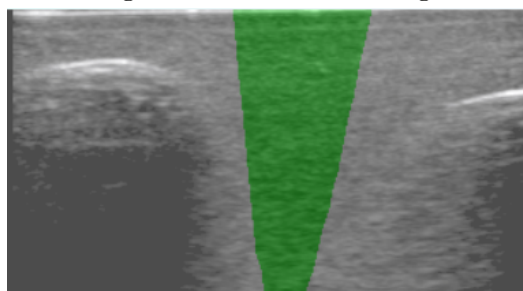
(c) Safe Area (in green) Overlayed with the Input Ultrasound Image

Fig. 3.12 Results

Chapter 4

Results & Discussions

4.1 Results

4.1.1 Overlayed Safe Region

From 3.4.2 the entire process was followed for a dynamic data collection. As the images and the probe poses were captured, the ultrasound image was then labelled with a "safe insertion region" in green across the ultrasound image. Figure 4.1 shows a series of images taken during dynamic scanning of the lumbar spine. Right column shows the safe area overlayed on the captured ultrasound image, whereas the left column shows its corresponding MRI slice taken from the ground truth point cloud using the acquired ($^{\text{world}}T_{\text{MRI}}$).

4.2 Quantification of Results

For quantification of the accuracy of edge detection and $^{\text{world}}T_{\text{MRI}}$ calculation employed in Chapter 3, a method of generating corresponding MRI-US slices and finding the Intersection of Union (IoU) between them was employed.
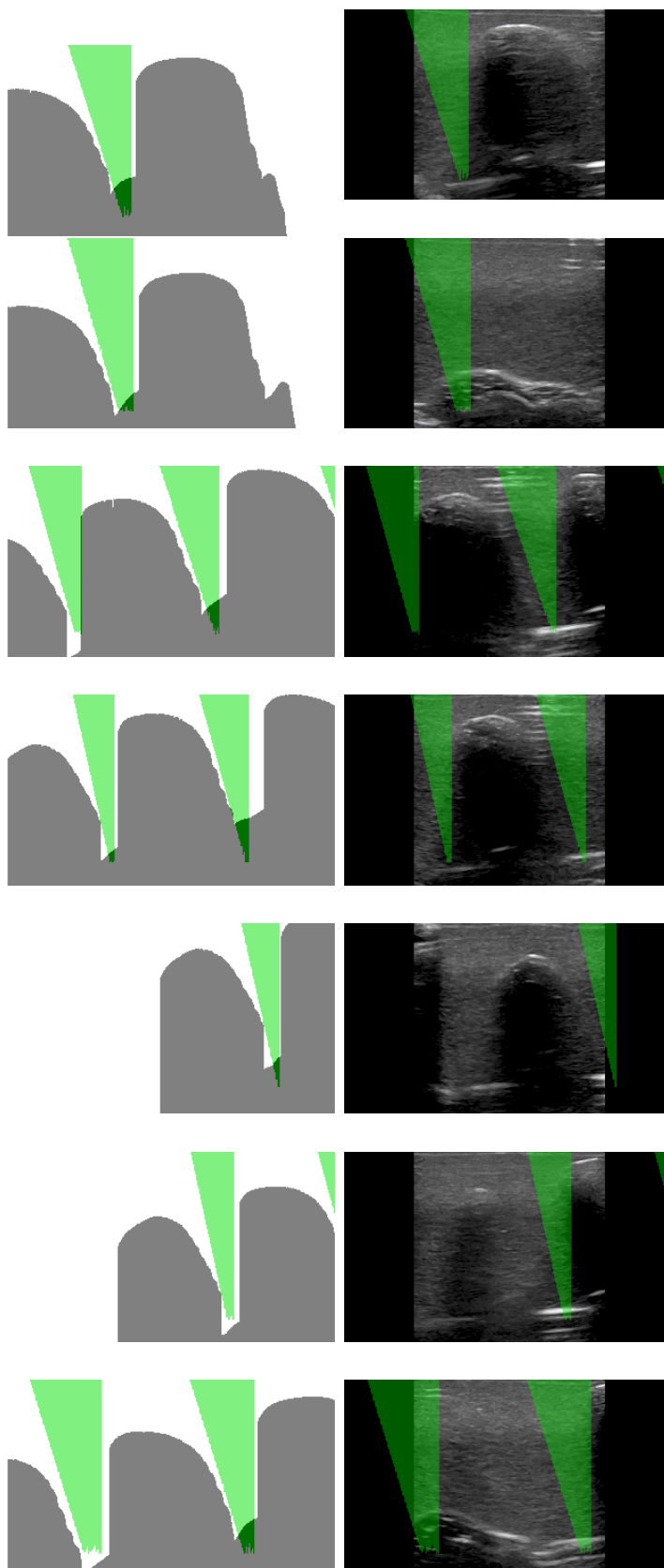
Fig. 4.1 MRI Slice (left) and Ultrasound Image (right) with Overlayed Safe Region

The IoU metric is used to evaluate the overlap between the areas given two images. In the context of my research, IoU has been used to measure the volumetric overlap between the MRI and US point clouds after registration, for before local optimization and after local optimization. A higher IoU percentage indicates a greater degree of overlap and, by implication, a more accurate registration.

The accuracy calculation was done on 44 dynamically captured ultrasound images using vertical placement of the probe. The images were taken by placing the probe vertically and scanning the lumbar vertebrae. The images were purposely taken such that the edges were unclear and some bones were obscured. The IoU calculation was performed between ultrasound and corresponding MRI mask. The ultrasound mask was taken by detecting edges, and marking all image points under those edges as bone-points, while MRI mask was the MRI bones slice we obtained with the same method as in Section 3.3.3. Thus, in simple words, IoU was calculate between bone-points in the two masks.

The $^{\text{world}}T_{\text{MRI}}$ for this set of experiment was done on a dataset with images taken by horizontally placing the probe. The IoU percentage of the images was calculated before and after local optimization in the dynamic process. Figure 4.2 shows the IoU percentages of 44 images before and after optimization. The average overlap percentage before local optimization came to be 72.15%, while after optimization was 85.35%.

4.3   Discussions

This research provides a dynamic overlay of safe insertion regions upon capturing ultrasound images, along with an estimate of the transformation for ground truth with respect to the world frame, $^{\text{world}}T_{\text{MRI}}$. Thus, we get a visualization tool which can guide practitioners during procedures, offering real-time visuals for a defined safe needle insertion pathway.
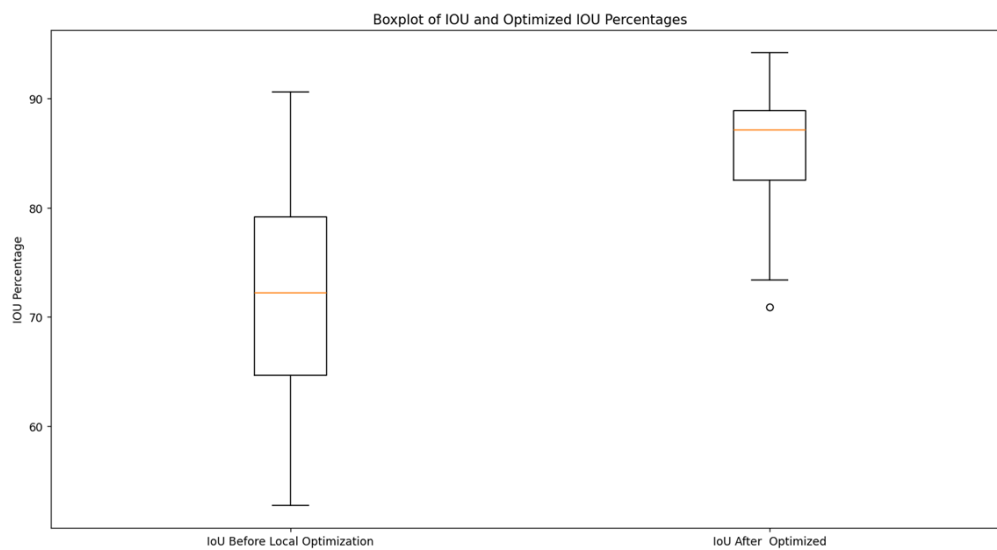
Fig. 4.2 Box Plot showing IoU Percentage for Ultrasound and MRI Masks Before and After Localization for 44 Images Captured
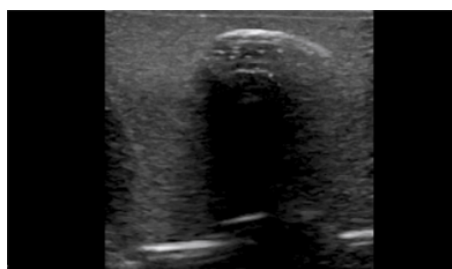
Overlap Before Optimization
70.417%

Overlap After Optimization
87.831%

Fig. 4.3 IoU Visual results for an Image Before and After Optimization

Moreover, by defining an insertion point on the image, the transformation train enables the transposition of this point into the world coordinate system. This can allow for the calculations of the entry angle necessary to reach the defined target region within the spine.

Thus, this technique can be refined to help practitioners make decisions about the needle's insertion point and trajectory, adjusting their technique to account for patient-specific anatomy and the location of safe zones.

By integrating our methodology into the clinical workflow, we think that it can serve in reducing learning and procedure times, contributing to better outcomes.

Chapter 5

Conclusion and Future Work

5.1 Conclusion

In conclusion, this thesis integrated ultrasound imaging data with corresponding probe position information to construct a transformation framework that aligns with MRI ground truth data. The first step in this process involved identifying bone edges using a classical intensity-based edge detection algorithm, which was then translated into a world coordinate frame. This allowed us to create a sparse ultrasound-based point cloud that could be registered to the MRI ground truth model.

With localization of the ultrasound probe in relation to the MRI data established, we were able to superimpose the predetermined safe regions from the MRI onto the ultrasound images. This step was added with a local optimization process, enhancing the refinement and accuracy of our registration.

With the transformation train already established, further advancements can be made by defining precise needle entry and target points within the MRI ground truth. This approach allows for each entry point to be transformed directly into a corresponding point on the patient's body in the real world, complete with a specified angle for needle insertion. This means that whenever an ultrasound image is captured

and identifies a safe insertion region, the system can not only suggest an an insertion point on the body but also provide the appropriate angle for insertion. Implementing this guidance means that if the needle inserted correctly at the indicated point and angle, will reach the targeted location inside the body.

A complete workflow of our thesis, which encapsulates the methodologies and steps of this study, is illustrated in Figure 5.1.
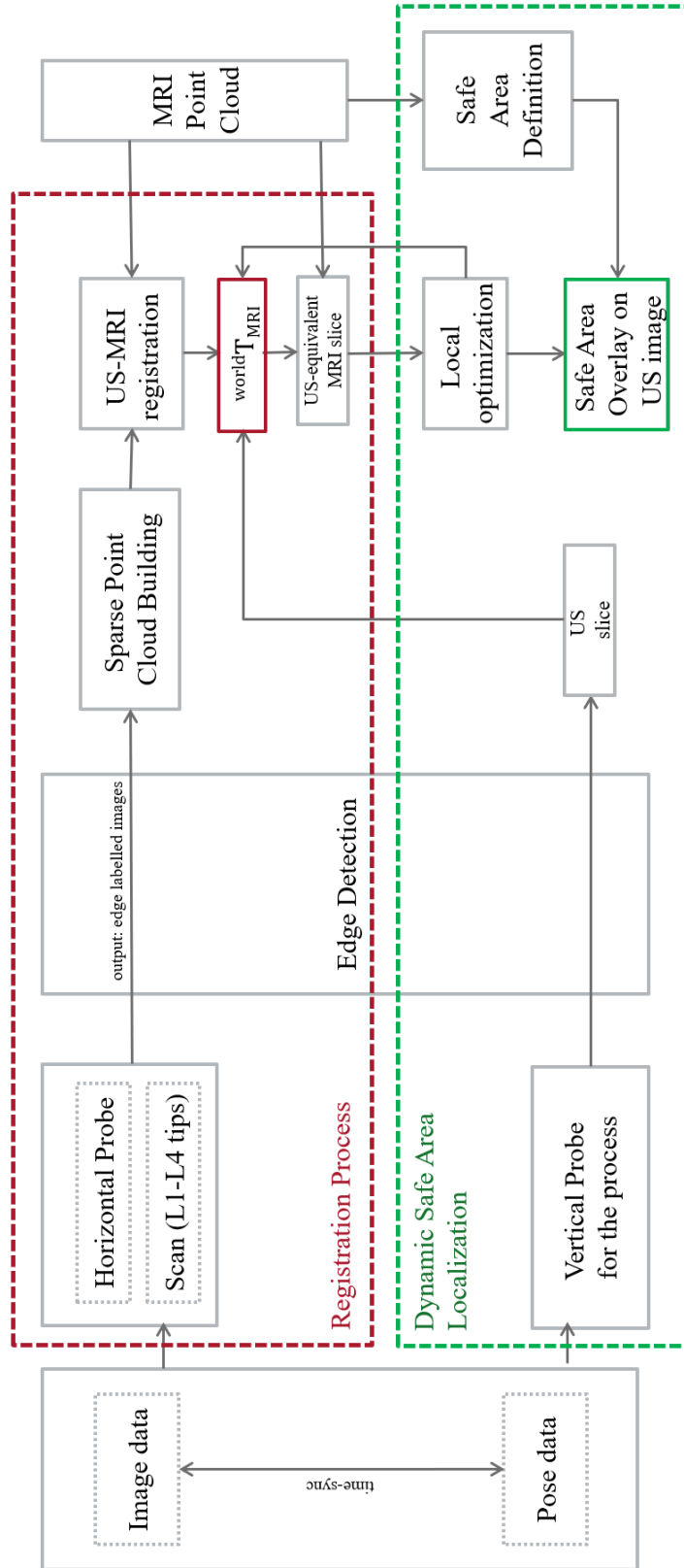
Fig. 5.1 Framework for the the Process

5.2 Future Work and Directions

While this study has established a method for lumbar puncture and epidural guidance using MRI as a ground truth, it is important to recognize that obtaining MRI scans prior to these procedures is not always practical or feasible in a clinical setting. Therefore, a primary objective for future research is to develop a scalable model derived from a generalized ground truth. This model would be adaptable to individual patient anatomy, and can be used for registration during procedures without the need for pre-operative imaging.

Additionally, while the VICON motion capture system has provided accurate tracking within a research environment, its application in the space-constrained medical settings is challenging. As an alternative, stick-on Inertial Measurement Units (IMUs) could be explored for their potential to track the ultrasound probe with similar precision yet greater ease of use in clinical practice.

Furthermore, the current local optimization process is limited to the x-y plane, aligning with the plane of the ultrasound image. However, in real-world scenarios, patient movement may occur in three dimensions. Future iterations of this optimization process must account for shifts along the z-axis, thereby offering a more robust and comprehensive solution that can accommodate the full range of patient movement during procedures.

Implementing these advancements will help to obtain more versatile and practical application of the techniques developed in this thesis, ultimately improving the standard of care provided to patients undergoing lumbar punctures and epidural anesthesia.

References

[1] Baka, N., Leenstra, S., and van Walsum, T. (2017a). Ultrasound aided vertebral level localization for lumbar surgery. *IEEE Transactions on Medical Imaging*, 36(10):2138–2147.

[2] Baka, N., Leenstra, S., and van Walsum, T. (2017b). Ultrasound aided vertebral level localization for lumbar surgery. *IEEE Transactions on Medical Imaging*, 36(10):2138–2147.

[3] Boon, J., Abrahams, P., Meiring, J., and Welch, T. (2004a). Lumbar puncture: Anatomical review of a clinical skill. *Clinical Anatomy*, 17(7):544–553.

[4] Boon, J. M., Abrahams, P. H., Meiring, J. H., and Welch, T. (2004b). Lumbar puncture: Anatomical review of a clinical skill. *Clinical Anatomy*, 17:544–553.

[5] Brattain, L. J., Floryan, C., Hauser, O. P., Nguyen, M., Yong, R. J., Kesner, S. B., Corn, S. B., and Walsh, C. J. (2011). Simple and effective ultrasound needle guidance system. In *2011 Annual International Conference of the IEEE Engineering in Medicine and Biology Society*, pages 8090–8093.

[6] Busti, A. J. and Kellogg, D. (2015). Procedure: Lumbar puncture. EBM Consult. Copyright EBM Consult, LLC. Last reviewed August 2015.

[7] Clerk Maxwell, J. (1892). *A Treatise on Electricity and Magnetism*, volume 2. Oxford: Clarendon, 3rd edition.

[8] Doherty, C. and Forbes, R. (2014). Diagnostic lumbar puncture. *Ulster Med J*, 83(2):93–102.

[9] Hermanides, J., Hollmann, M., Stevens, M., and Lirk, P. (2012). Failed epidural: Causes and management. *BJA: British Journal of Anaesthesia*, 109(2):144–154.

[10] Johnson, D., Waid, M., Rula, E., Hughes, D., Rosenkrantz, A., and Duszak, R. (2021). Comparison of radiologists and other specialists in the performance of lumbar puncture procedures over time. 42(6):1174–1181.

[11] Kerby, B., Rohling, R., Nair, V., and Abolmaesumi, P. (2008). Automatic identification of lumbar level with ultrasound. In *2008 30th Annual International Conference of the IEEE Engineering in Medicine and Biology Society*, pages 2980–2983.

[12] Li, H., Wang, Y., Li, Y., and Zhang, J. (2021). A novel manipulator with needle insertion forces feedback for robot-assisted lumbar puncture. *International Journal of Medical Robotics and Computer Assisted Surgery*, 17(2):e2226.

[13] Mofidi, M., Mohammadi, M., Saidi, H., Kianmehr, N., Ghasemi, A., Hafezi-moghadam, P., and Rezai, M. (2013). Ultrasound guided lumbar puncture in emergency department: Time saving and less complications. *Journal of Research in Medical Sciences*, 18(4):303–307.

[14] Rankin, J. H., Elkhunovich, M. A., Rangarajan, V., Chilstrom, M., and Mailhot, T. (2016). Learning curves for ultrasound assessment of lumbar puncture insertion sites: When is competency established? *The Journal of Emergency Medicine*, 51(1):55–62.

[15] Shajudeen, P. M. S. and Righetti, R. (2017). Spine surface detection from local phase-symmetry enhanced ridges in ultrasound images. *Medical Physics*, 44(11):5755–5767.

[16] Short, A., Dunneback, E., Stephens, J. R., Guidici, J., Chatterjee, A., Finn, E., Contarino, M., Spangler, H., Heath, J., McEntee, J., Donohoe, A., Hemsey, D., Moore, C., Sturkie, E., Kumfer, A. M., Campbell, R. A., and Dancel, R. (2023). Safety and predictors of the success of lumbar punctures performed by a medicine procedure service. *Journal of Hospital Medicine*, 18:661–669.

[17] Tiouririne, M., Dixon, A. J., Mauldin Jr, F. W., Scalzo, D., and Krishnaraj, A. (2017). Imaging performance of a handheld ultrasound system with real-time computer-aided detection of lumbar spine anatomy: A feasibility study. *Investigative Radiology*, 52(8):447–455.

[18] Tran, D. and Rohling, R. N. (2010). Automatic detection of lumbar anatomy in ultrasound images of human subjects. *IEEE Transactions on Biomedical Engineering*, 57(9):2248–2256.

[19] Vickers, A., Donnelly, J. P., Moore, J. X., Barnum, S. R., Schein, T. N., and Wang, H. E. (2018). Epidemiology of lumbar punctures in hospitalized patients in the united states. *PLoS ONE*, 13(12):e0208622.

[20] Yu, S., Tan, K. K., Sng, B. L., Li, S., and Sia, A. T. H. (2015). Lumbar ultrasound image feature extraction and classification with support vector machine. *Ultrasound in Medicine & Biology*, 41(10):2677–2689.

Appendix A

Appendix

The appendix involves some calculations done in the establishment of co-ordinate frame relations within the thesis.

A.0.1   Data Generation for Vicon Markers

This section provides the calculation for constructing a transformation matrix needed to align the poses three Vicon markers with any origin.

Given three marker positions, marker1, marker2, and marker3, the function first computes the centroid of these markers to establish a local coordinate system. The centroid is calculated as the mean of the marker positions.

$$\begin{bmatrix} \text{c1} & \text{c2} & \text{c3} \end{bmatrix} = \frac{1}{3}(\texttt{marker1} + \texttt{marker3} + \texttt{marker3}) \tag{A.1}$$

Using the centroid, the relative position vectors of $\texttt{m1}$ and $\texttt{m2}$ with respect to the centroid are determined, and then they are normalized to form the basis vectors of the local coordinate system.

$$nv1 = \texttt{marker1} - \text{centroid} \tag{A.2}$$

$$nv2 = \texttt{marker2} - \text{centroid} \tag{A.3}$$

$$xc = \frac{nv1}{\|nv1\|} \tag{A.4}$$

$$rc = \frac{nv2}{\|nv2\|} \tag{A.5}$$

The orthogonal basis vector zc is computed by taking the cross product of xc and rc, then normalizing the result.

$$zc = \frac{xc \times rc}{\|xc \times rc\|} \tag{A.6}$$

The final basis vector yc is determined by the cross product of zc and xc to ensure orthogonality and right-handed coordinate system, followed by normalization.

$$yc = \frac{zc \times xc}{\|zc \times xc\|} \tag{A.7}$$

These basis vectors xc, yc, and zc form the rotation matrix of the transformation. The centroid co-ordinates form the translation matrix of the transformation.

Thus, the transformation matrix for centroid to origin alignment is given by:

$$^{\text{origin}}T_{\text{centroid}} = \begin{bmatrix} \text{R} & \text{c} \\ 0 & 1 \end{bmatrix} \tag{A.8}$$

where $R = \begin{bmatrix} \text{xc} & \text{yc} & \text{zc} \end{bmatrix}$, and $c = \begin{bmatrix} \text{c1} & \text{c2} & \text{c3} \end{bmatrix}$, from Equation A.1.